

## Research Article

# Pore Structure Alteration Characteristics of Different Mineralogical Composition Shale during Shale-Fracturing Fluid Physical-Chemical Interactions

Zepeng Sun<sup>1</sup>, Yongli Wang<sup>2</sup>, Zhifu Wei<sup>3</sup>, Yue Ni<sup>1</sup>, Baoxiang Wu<sup>3</sup>, Jing Li<sup>3</sup>, Wenhua Fan<sup>1</sup>, Gailing Wang<sup>1</sup> and Yunxiao Li<sup>1</sup>

<sup>1</sup>College of Resource and Environment, Shanxi Agricultural University, Taigu 030801, China

<sup>2</sup>Key Laboratory of Cenozoic Geology and Environment, Institute of Geology and Geophysics, Chinese Academy of Sciences, CAS Center for Excellence in Life and Paleoenvironment, Beijing 100029, China

<sup>3</sup>Key Laboratory of Petroleum Resources Research, Gansu Province, Northwest Institute of Eco-Environment and Resources, Chinese Academy of Sciences, Lanzhou 730000, China

Correspondence should be addressed to Yongli Wang; [ylwang@mail.iggcas.ac.cn](mailto:ylwang@mail.iggcas.ac.cn) and Zhifu Wei; [weizf@lzb.ac.cn](mailto:weizf@lzb.ac.cn)

Received 10 April 2019; Revised 12 July 2019; Accepted 11 September 2019; Published 15 November 2019

Academic Editor: Shengnan Nancy Chen

Copyright © 2019 Zepeng Sun et al. This is an open access article distributed under the Creative Commons Attribution License, which permits unrestricted use, distribution, and reproduction in any medium, provided the original work is properly cited.

Hydraulic fracturing is widely applied to economic gas production from shale reservoirs, but the effect of the shale mineral composition on the physical-chemical reactions during hydraulic fracturing is still poorly understood. To develop a foundational understanding of chemical interactions occurring on shale with different mineralogical compositions, two different types of mineral composition marine shale (carbonate-poor and carbonate-rich) from the Niutitang Formation were reacted with slick water fracturing fluid in a laboratory reactor at 100°C and 50 MPa for three days. To identify the changes of the pore structure characteristics during hydraulic fracturing, the field emission scanning electron microscopy (FE-SEM), X-ray diffraction (XRD), low-temperature nitrogen adsorption, and porosity measurement were performed on the original and treated shale samples. After the slick water treatment, the dissolution of pyrite in carbonate-poor shale (obtained from Youyang County, labeled as YY) was observed by FE-SEM and XRD analyses, while in carbonate-rich shale (obtained from Guzhang County, labeled as GZ), the carbonate dissolution was observed. Results from the low-temperature N<sub>2</sub> adsorption and porosity measurement demonstrated that the variation trend of pore structure characteristics for the YY and GZ shale samples was quite different after reacting with slick water fracturing fluid. For YY shale, the specific surface area, total pore volume, and porosity increased after the reaction, whereas an opposite trend was observed in the GZ shale. Moreover, the fractal dimension analysis illustrated that the pore surface became less rough and the pore structure became more complex in the YY shale, whereas the degree of pore surface roughness and pore structure complexity of the GZ shale was reduced. The results demonstrated that the initial mineralogical composition of shale played an important role in pore structure alteration during hydraulic fracturing.

## 1. Introduction

Unconventional shale gas exploitation from low-permeability shale reservoir rocks has increased worldwide over the last decade owing to the comprehensive development of multistage hydraulic fracturing and horizontal well-drilling technologies [1, 2]. According to the data of the U.S. Energy Information Administration (EIA), Ameri-

can shale gas production accounts for 50% of total natural gas production which exceeded  $4.2 \times 10^{11} \text{ m}^3$  in 2015 [3]. In addition, China, Canada, and Australia, among other countries, are also developing programs to exploit shale gas resources [4]. After nearly ten years of exploration and research, China has constructed four major marine shale gas fields including Changning, Zhaotong, Weiyuan, and Jiaoshiba in the southern Sichuan Basin [5, 6]. By the

end of 2017, the shale gas annual industrial production was  $9.1 \times 10^9 \text{ m}^3$ , which showed a rapid increase within a short period of China's shale gas exploration and development [6].

Through hydraulic fracturing operations, the high-pressure fracturing fluids are injected into the shale formation, thus not only releasing the adsorbed gas but also creating complex fracture networks for gas transport [7]. However, approximately more than 50% of the fracturing fluid was retained in the shale formation [8, 9]. These trapped fracturing fluids could interact with the shale formation and affect the reservoir permeability and productivity [10]. Many studies have discussed the clay-swelling and water-blocking effects of shale formation by spontaneous imbibition experiments [9, 11, 12]. The clay swelling and water blocks will hinder the gas flow and result in the effective permeability reduction of shale [13]. Meanwhile, the mineral particle jointing strength will be weakened through the hydration, which further decreases the conductivity of prop fractures [14]. Although experiments of water-rock interactions at the laboratory scale offered valuable preliminary data on physical-chemical interactions between shale and fracturing fluid, most of these imbibition experiments were performed at low temperature and low pressure [15–17]. Considering that the reservoir usually has high-temperature and high-pressure conditions [18], the experiments performed at reservoir temperature and pressure are more approximate conditions in the field [19].

Many specific chemical additives are added in the fracturing fluid to increase the shale gas production, resulting in the fact that the fracturing fluid is acidic and oxidic [20]. In our previous study, we found that the 2-acrylamido-2-methyl-propane sulfonic acid in the friction reducer of the slick water fracturing fluid could cause the carbonate mineral dissolution of shale formation rocks [21]. Moreover, the adsorption of polymer in the slick water fracturing fluid broke the molecular structure of the anionic polyacrylamide and further resulted in the reduction of pore throat radius of shale [22]. Pearce et al. [23] reported that the interactions between shale and fracturing fluid could cause the precipitation of Fe oxides, which could clog pore throats or fractures, and decrease the long-term gas production. The chemical reactions occurring on the shale gas reservoir can alter the wettability and pore structure of shale, which can in turn alter the shale gas transport behavior and affect the shale gas production ultimately [24]. Therefore, investigating the geochemical interactions between shale reservoir rocks and fracturing fluid are important to effectively manage the shale gas production and to optimize the chemistry composition of the fracturing fluid for shale gas stimulation.

Although hydraulic fracturing technology for shale gas production is ubiquitous at present, little is known about the geochemical reactions and physical changes during shale-hydraulic fracturing fluid reactions and factors that control these reactions. Therefore, in this study, we investigate the reactions happening between slick water fracturing fluid and shale with different mineralogical compositions

under reservoir temperature and fracturing pressure. The primary objectives of this study are to evaluate the influence of different mineralogical compositions on the changes of pore structure characteristics and porosity of shale during interaction with hydraulic fracturing fluid.

## 2. Materials and Methods

*2.1. Shale Samples.* In this research, two different mineral composition marine shale samples of the Lower Cambrian Niutitang Formation were obtained from Youyang County in the southeastern Chongqing area (labeled as YY) and Guzhang County in the northwestern Hunan area (labeled as GZ) (Figure 1). The two shale samples were obtained from the outcrops of their sections, and only the fresh samples were collected during the mining. All analyses were performed at the Key Laboratory of Petroleum Resources, Gansu Province.

The geochemical characteristics and initial mineralogical compositions of the two studied shale samples are listed in Table 1. These two kinds of shale samples showed high total organic carbon (TOC) content, with the value of 8.42% (YY) and 6.26% (GZ). The carbon isotope ratios of organic matter ( $\delta^{13}\text{C}_{\text{org}}$ ) of the two shale samples were  $-31.8\text{‰}$  (YY) and  $-32.8\text{‰}$  (GZ), and the low  $\delta^{13}\text{C}_{\text{org}}$  value may be related to the anoxic conditions of the sedimentary environment [25]. As shown in Table 1, the main minerals of YY shale were quartz (65%), clay minerals (14%), and feldspar (11%), with a small amount of pyrite (8%) and carbonate minerals (calcite+dolomite) (2%). However, the main minerals of GZ shale were carbonate minerals (68%), quartz (15%), and pyrite (10%), with a small amount of clay minerals (4%) and feldspar (3%). Depending on the mineralogical characteristics of the two shale samples, we separated the two shale samples into carbonate-poor (YY) and carbonate-rich (GZ) categories.

For different measurement purposes, the two bulk shale samples were drilled and broken to different sizes. The core samples with size of 2.5 cm diameter and 5.0 cm length were drilled from the blocks and prepared for the porosity test. Meanwhile, small cubes with size of 2–3  $\text{cm}^3$  were obtained for FE-SEM analysis. Besides, over 100 g of fragments obtained from adjacent offcuts were crushed to 40–60 mesh for XRD and low-temperature  $\text{N}_2$  adsorption measurement. Before the experiment, all the prepared shale samples were cleaned using clean water which was a colorless, transparent, tasteless, and neutral liquid and then dried at  $50^\circ\text{C}$  for 12 hours in the oven to remove the moisture in the samples.

In this experiment, one of the most commonly used water-based hydraulic fracturing fluids, slick water fracturing fluid, was used. The chemical components and physical property of the slick water fracturing fluid are shown in Table 2.

*2.2. Experimental Procedure.* The influence of the mineralogical composition on the evolution of shale reservoir pore structure characteristics under the injection of slick water fracturing fluid was studied using a high-temperature and high-pressure reactor device (Figure 2). The apparatus, which was described in detail previously [21], includes a

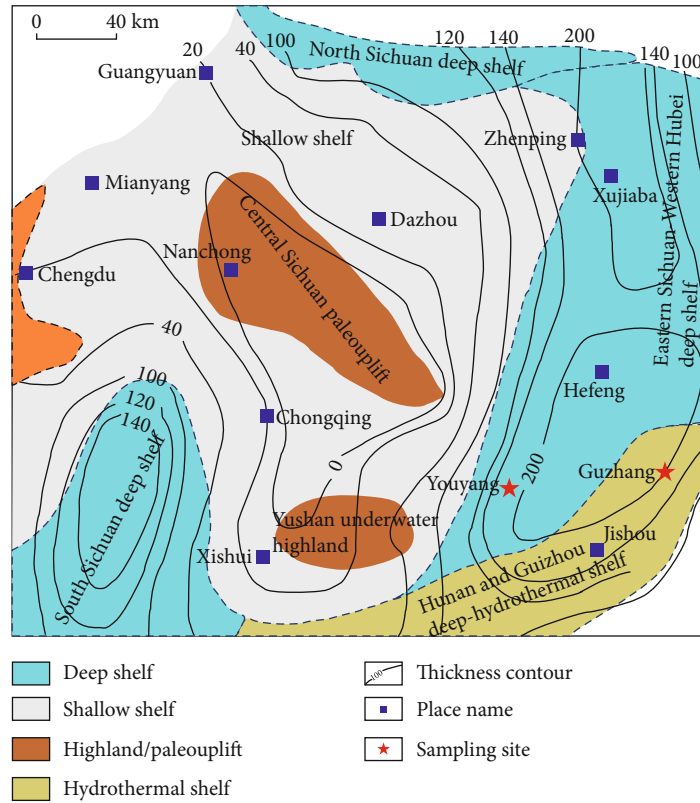


FIGURE 1: The thickness of the Lower Cambrian shale on the Middle and Upper Yangtze and the sampling sites (modified after [26]).

TABLE 1: Geochemical data and initial mineralogical composition of the two shale samples.

| Sample | TOC (%) | $\delta^{13}C_{org}$ (‰) | Mineral composition (%) |         |          |        |          |               |
|--------|---------|--------------------------|-------------------------|---------|----------|--------|----------|---------------|
|        |         |                          | Quartz                  | Calcite | Dolomite | Pyrite | Feldspar | Clay minerals |
| YY     | 8.42    | -31.8                    | 65                      | 1       | 1        | 8      | 11       | 14            |
| GZ     | 6.26    | -32.8                    | 15                      | 8       | 60       | 10     | 3        | 4             |

TABLE 2: Components and physical property of the slick water fracturing fluid.

| Component        |                    |               |             | Physical property |                 |                       |
|------------------|--------------------|---------------|-------------|-------------------|-----------------|-----------------------|
| Friction reducer | Clay control agent | Cleanup agent | Demulsifier | pH                | Surface tension | Wetting contact angle |
| 0.2 wt. %        | 1 wt. %            | 0.15 wt. %    | 0.05 wt. %  | 5.23              | 29.31 mN/m      | 60.11°                |

reactor (500 ml), constant speed and pressure pump, vacuum pump, and piston container.

All experiments were conducted at reservoir temperature (100°C) according to the depth of shale formation in Niutang (the burial depth is 3-4 km [27]) and fracturing pressure (50 MPa). In order to investigate the effects of fracturing fluid initially entering the shale reservoir, the reaction time was set at three days. The experiment included the following steps: (1) shale samples with different sizes (cylinder, cube, and 40-60 mesh) were placed into the reactor, (2) the slick water fracturing fluid was poured in, and (3) reaction conditions

were set for three days, at 100°C and 50 MPa. In addition, the fracturing fluid of 10 ml was sampled during the experiments at 24 h, 48 h, and 72 h, which were used for measuring the pH value. After reaction, the shale samples were taken out of the fracturing fluid, cleaned using ultrapure deionized water, and then dried at the condition of 50°C for 12 hours in the oven. Before and after the interaction, the mineral composition, pore structure characteristics, and porosity were measured.

The mineral compositions of shale samples before and after reaction were measured using a Rigaku D/Max-III B

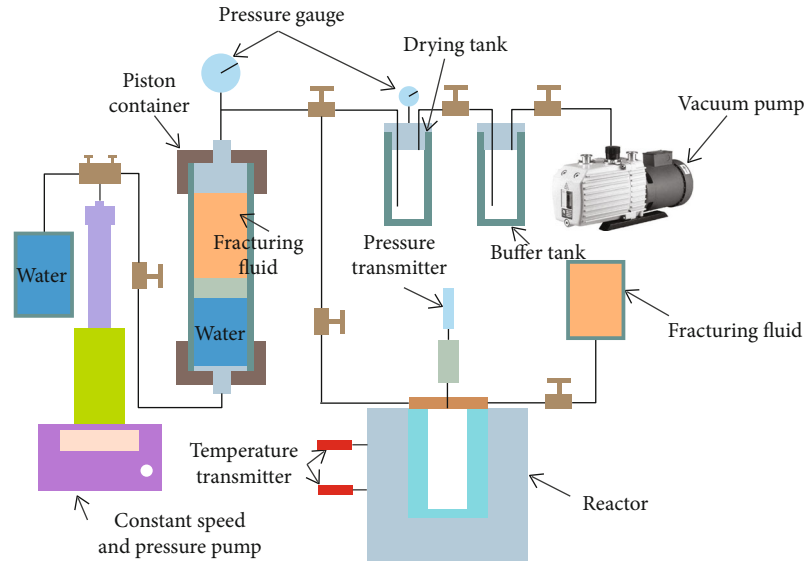


FIGURE 2: Schematic diagram of the experiment instrument [21].

X-ray diffractometer, at 40 kV and 40 mA with a Cu  $K\alpha$  radiation, and then scanned from  $3^\circ$  to  $70^\circ$  at a rate of  $2.0^\circ/\text{min}$ . The 40-60 mesh shale samples were crushed into 200-300 mesh for XRD analysis following the Chinese Oil and Gas Industry Standards SY/T5983-1994 and SY/T5163-1995.

A field emission scanning electron microscope with an energy-dispersive X-ray spectroscopy (Zeiss, Merlin Compact) was used to identify the changes of mineralogy of the shale samples before and after reaction. To minimize the effect of the artifacts and roughness of the shale surface on the FE-SEM observation, the shale sample surfaces were polished using an argon ion mill (Gatan, PECS II model 685 cross-section polisher).

Low-temperature nitrogen adsorption analyses were carried out on an ASAP 2020 HD88 surface area analyzer. The 40-60-mesh shale samples with approximately 0.3 g were automatically degassed at  $110^\circ\text{C}$  in a vacuum for 20 h to remove adsorbed moisture and gaseous impurities. Then, the degassed samples were kept at the temperature of liquid nitrogen temperature ( $-196^\circ\text{C}$ ). The relative equilibrium adsorption pressure ( $P/P_0$ ) for nitrogen adsorption ranged from 0.009 to 0.995 ( $P$ : actual gas pressure;  $P_0$ : saturation pressure). The multipoint Brunauer-Emmett-Teller (BET) equation was used to calculate the specific surface area [28], and the Barrett-Joyner-Halenda (BJH) method was used to calculate the pore volume and pore size distribution [29].

The porosity of shale samples was measured by a PoroPDP-200 porosity tester, and we chose the core samples without visible cracks in order to increase measuring accuracy. The porosity was calculated using the principle of helium gas expansion, and operation pressure ranged from 0 to 0.7 MPa.

### 3. Results and Discussions

**3.1. FE-SEM Analysis.** The surface pore structure of the two shale samples before and after treatment with slick water fracturing fluid is shown in the FE-SEM images (Figures 3

and 4). In the raw carbonate-poor shale sample (YY), the interparticle (interP) and intraparticle (intraP) pores were observed (Figures 3(a) and 3(b)). The interP pores were found between different mineral particles, and the intraP pores were distributed within incompletely filled quartz and calcite (Figures 3(a) and 3(b)). Moreover, organoclay complex pores were identified between the organic matter and clay minerals (Figure 3(b)). However, the pyrite dissolution and clay swelling were observed after the interaction with slick water for three days (Figures 3(c) and 3(d)), which altered the surface morphology of shale. In addition, some new fractures were formed surrounding the pyrite (Figure 3(c)), and organoclay complex pores were destroyed due to the water adsorption-induced clay swelling.

In the raw carbonate-rich shale sample (GZ), the interP pores were identified around different mineral particles and the intraP pores were developed in pyrite and quartz (Figures 4(a) and 4(b)). However, after the slick water treatment, some dissolution pores and stripes were formed due to the carbonate dissolution (Figures 4(c) and 4(d)). Moreover, the collapse and roughness in the mixed zone of carbonate and other minerals were formed after the reaction. The reasons for the different changes of surface pore structure of the two shale samples will be discussed later in this paper.

**3.2. XRD Analysis.** The mineralogical composition of the two shale samples before and after reaction with slick water is presented in Table 3. As seen in Table 3, the two shale samples showed different variation characteristics after interaction with slick water. In the YY shale sample, the pyrite content decreased by 25% (from 8% to 6%), while the clay mineral content increased by 14.3% (from 14% to 16%). In contrast to the changes of pyrite and clay minerals, the content of quartz showed slight changes, and the feldspar and dolomite were not changed. In addition, the calcite was not detected after reaction. In the GZ shale sample, the calcite content obviously decreased by 62.5% (from 8% to 3%) after

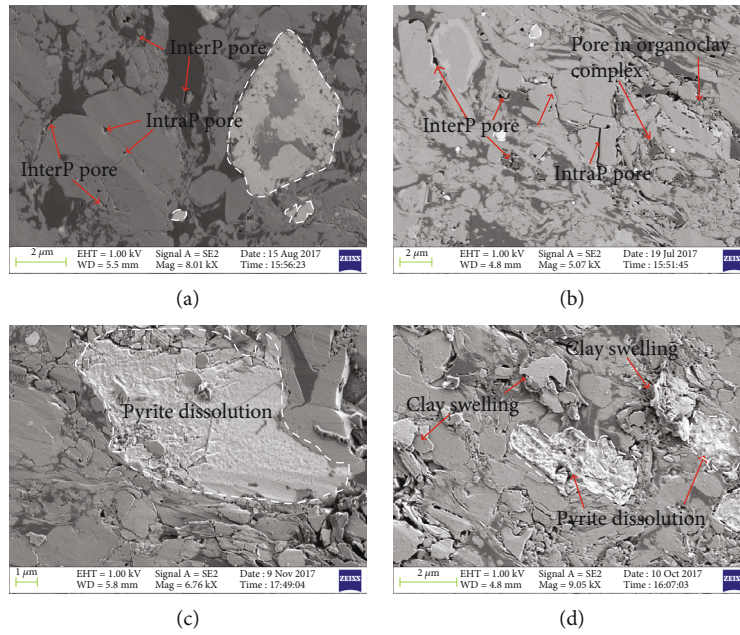


FIGURE 3: Field emission scanning electron microscope (FE-SEM) images of raw (a, b) and treated (c, d) YY shale (the white marks are the pyrite location).

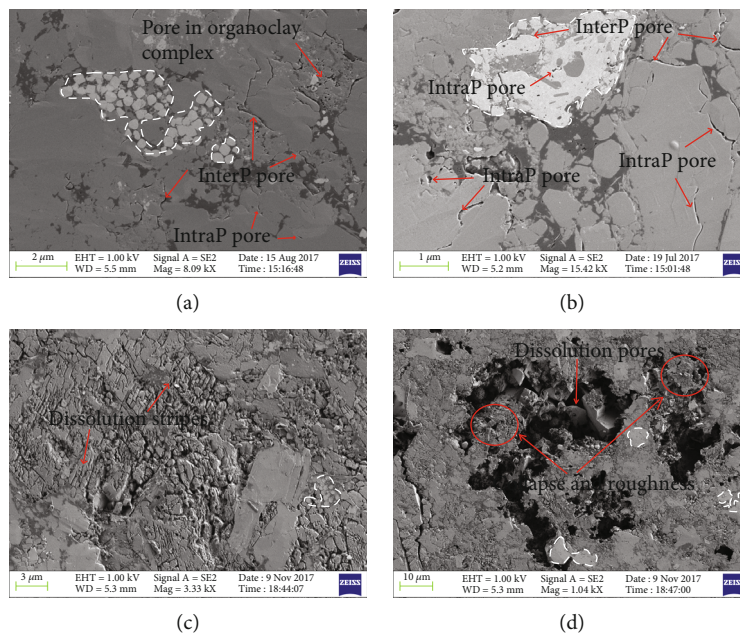


FIGURE 4: Field emission scanning electron microscope (FE-SEM) images of raw (a, b) and treated (c, d) GZ shale (the white marks are the pyrite location).

reacting with slick water, and the content of dolomite decreased from 60% to 55%. Conversely, the content of quartz, pyrite, plagioclase, and clay minerals showed an increasing trend with decreasing carbonate mineral (calcite +dolomite) content. The increase of quartz, pyrite, and plagioclase of GZ shale may be related to the renormalization of the remaining phases following the decrease of carbonate minerals from the shale samples owing to the dissolution.

Previous studies showed that illite, mixed layer illite/smectite, and chlorites were the dominant clay minerals in the shale of the Niutitang Formation in Youyang County and Northwest Hunan area [30, 31] and that the illite/smectite mixed layer mineral possessed strong water imbibition capacity [14]. Therefore, the clay osmotic swelling would occur after the shale samples reacted with the slick water fracturing fluid, and the adsorbed water by clay minerals

TABLE 3: Mineralogical compositions of the shale samples before and after slick water treatment (%).

| Samples | State   | Quartz | Calcite | Dolomite | Pyrite | Plagioclase | Clay minerals |
|---------|---------|--------|---------|----------|--------|-------------|---------------|
| YY      | Raw     | 65     | 1       | 1        | 8      | 11          | 14            |
|         | Treated | 66     | 0       | 1        | 6      | 11          | 16            |
| GZ      | Raw     | 15     | 8       | 60       | 10     | 3           | 4             |
|         | Treated | 18     | 3       | 55       | 11     | 5           | 8             |

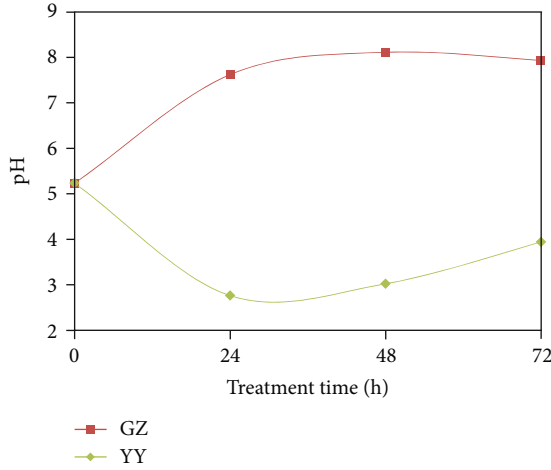
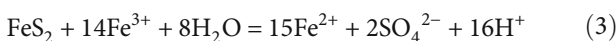
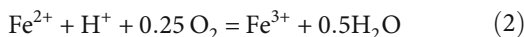
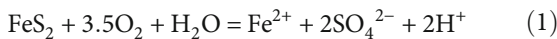


FIGURE 5: Changes of pH values during the reaction.

caused the expansion of a double diffusive layer of clay minerals [32]. Consequently, the clay swelling may lead to the increase of clay mineral content of carbonate-poor and carbonate-rich shale.

In all experiments, the pH values of the fluid were measured continuously during the reaction (Figure 5). In Figure 5, two distinct different trends in fluid pH were observed after the two shale samples reacted with slick water. The pH for the YY shale decreased rapidly after reacting for 24h (from 5.23 to 2.76), while gradually increased from 2.73 to 3.94 after 72h treatment. However, the GZ shale showed rapid pH increase from the value of 5.23 to 7.62 for the initial 24h of treatment, and the pH was stabilized at the value of 8 with increasing time. The changes of pH values and mineral compositions of shale samples may be related to the complicated chemical reactions induced by the slick water.

Previously, studies showed that the dissolved oxygen in the fracturing fluid could create an oxic condition in the shale reservoirs [19, 33]. Pyrite ( $\text{FeS}_2$ ) is a reductive sulfide with iron (II) which is stable only at very low oxidation states, and the pyrite in shale can be easily oxidized under the atmospheric oxygen and water environment [24, 34]. Overall, the reactions involved in pyrite oxidation are generally expressed by the following equations [35]:

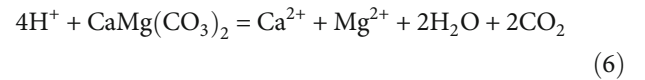
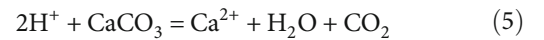


The oxygen required for pyrite oxidation could be carried alongside the fracturing fluid into the shale reservoir rocks [17]. Therefore, when the oxidative slick water reacted with the YY shale, the pyrite would undergo the oxidative dissolution and generate sulfate and acid (reactions (1)–(3)). Furthermore, the pyrite dissolution was observed with FE-SEM (Figures 3(c) and 3(d)), and the pyrite content decreased by 25% after reaction. From the reactions of (1) to (3), we can see that pyrite oxidation will release the ions of  $\text{H}^+$ , which accounts for the rapid decrease of pH value from 5.23 to 2.76 after reaction for 24h (Figure 5). Owing to the potential of the calcite to neutralize the  $\text{H}^+$  release during the pyrite dissolution [17, 36, 37], the buffering reaction of calcite for pyrite oxidation could be expressed by the following equation [17]:



Therefore, the acid generated from the pyrite oxidation caused the dissolution of calcite in YY shale, which may explain the increase of pH value from the 2.73 to 3.94 after 72h treatment (Figure 5).

In our previous study, we found that the hydrolysis of the 2-acrylamido-2-methyl-propane sulfonic acid (AMPS) in the friction reducer of slick water occurred during the reaction and released  $\text{H}^+$  [21]. For the carbonate-rich (GZ) shale, the dissolution of calcite and dolomite may be related to the following reactions:



From the reactions of (5) and (6), the GZ shale rapidly recovered the pH value of the fluid to neutral-alkaline condition.

In the study of Jew et al. [38], the release of Fe in the shale-hydraulic fracture fluid system was largely determined by the solution pH. The shale with abundant carbonates has high buffering capacity and shows lower overall release of  $\text{Fe}^{2+}$ . However, the shale with poor carbonates has low pH-buffering capacity, and the release of  $\text{Fe}^{2+}$  shows more stability [38]. Therefore, the different initial mineralogical compositions of the two shale samples (YY, GZ) resulted in the different chemical reactions during the reaction. The carbonate-poor YY shale had low pH-buffering capacity, causing the fluid pH to remain acidic

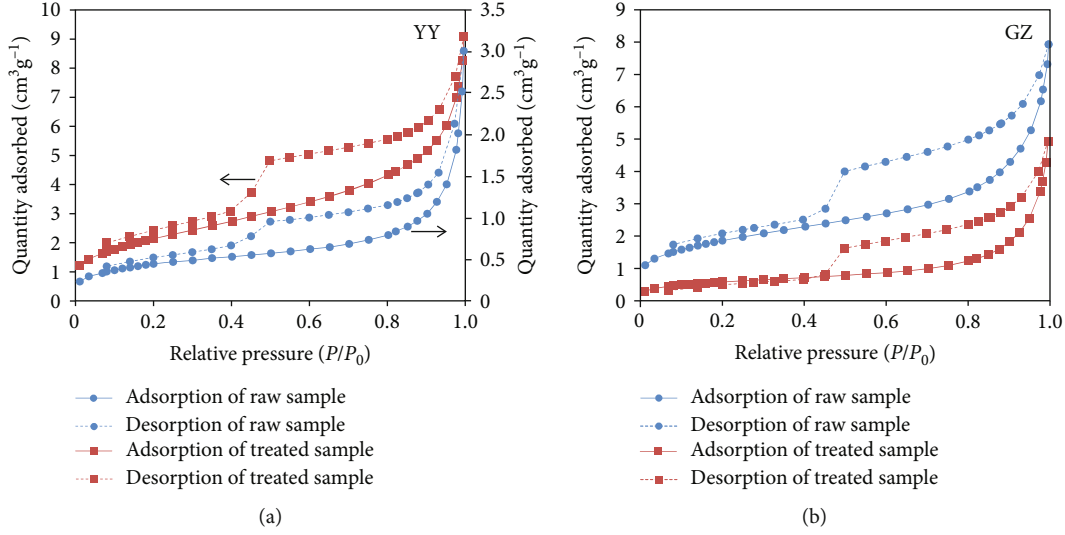


FIGURE 6: Low-temperature  $N_2$  adsorption-desorption isotherms of the two shale samples before and after reaction: (a) YY (arrows correspond to the ordinate); (b) GZ.

TABLE 4: Pore structure parameters of the shale samples before and after slick water treatment.

| Samples | State   | Specific surface area ( $m^2/g$ ) | Total pore volume ( $cm^3/g$ ) | Average pore diameter (nm) |
|---------|---------|-----------------------------------|--------------------------------|----------------------------|
| YY      | Raw     | 1.55                              | 0.00466                        | 11.99                      |
|         | Treated | 7.73                              | 0.01407                        | 7.28                       |
| GZ      | Raw     | 6.51                              | 0.01226                        | 7.54                       |
|         | Treated | 2.05                              | 0.00763                        | 14.87                      |

during reaction. Conversely, the carbonate-rich GZ shale had high pH-buffering capacity which can neutralize the  $H^+$  released from the hydrolysis of AMPS in the slick water and inhibited the dissolution of pyrite.

**3.3. Low-Temperature  $N_2$  Adsorption Analysis.** The shape of the low-temperature  $N_2$  adsorption-desorption isotherms and the hysteresis patterns can be effectively used to characterize the pore morphology of shale [31, 39]. Based on the classification of the International Union of Pure and Applied Chemistry (IUPAC), the isotherms can be classified into six types (I to VI), and the hysteresis patterns are designated H1 to H4 [40]. The isotherms of low  $N_2$  adsorption-desorption for the two shale samples before and after slick water treatment are presented in Figure 6. According to the classification of IUPAC, the  $N_2$  adsorption isotherms and the hysteresis pattern of all tested shale samples can be classified as Type IV isotherms and Type H2 hysteresis loops, respectively. The amount of adsorbed gas for all tested shale samples was low at a low relative pressure ( $P/P_0 < 0.01$ ), while the amount adsorbed increases steeply at a high relative pressure ( $P/P_0 > 0.9$ ). This phenomenon suggested that pores of these samples were mainly dominated by micropores ( $d < 2$  nm) and mesopores ( $d = 2 - 50$  nm), with few macropores ( $d > 50$  nm) [40]. Moreover, the Type H2 hysteresis loops of all tested shale samples indicated that the pore

shape of these shale samples may be inkbottle-shaped pores (with narrow necks and wide bodies) [40].

As seen in Figure 6, the shape of the isotherms showed a slight difference for the raw and slick water-treated shale samples. However, the maximum  $N_2$  quantity adsorbed at the highest pressure was changed. In the YY shale, the absorbed amount of  $N_2$  increased from  $3.01$   $cm^3/g$  to  $9.10$   $cm^3/g$ , reflecting that the  $N_2$ -adsorbed volume of shale was increased after the slick water treatment. Conversely, the maximum  $N_2$  quantity adsorbed decreased from  $7.93$   $cm^3/g$  to  $4.93$   $cm^3/g$  in the GZ shale, indicating that the  $N_2$  adsorption capacity of shale was decreased after reaction. The adsorption capacity was mainly related to the quantity of micropores and mesopores; therefore, the changes of the adsorbed  $N_2$  quantity of the two shale samples were attributed to the pore structure changes.

The pore parameters obtained from low-temperature  $N_2$  adsorption were presented in Table 4. The results showed that the specific surface area of YY shale increased from  $1.55$   $m^2/g$  to  $7.73$   $m^2/g$ , and the total pore volume increased from  $0.00466$   $cm^3/g$  to  $0.01407$   $cm^3/g$  after reaction with the slick water. However, for the GZ shale, specific surface area and total pore volume decreased after reaction, changing from  $6.51$   $m^2/g$  to  $2.05$   $m^2/g$  and from  $0.01226$   $cm^3/g$  to  $0.00763$   $cm^3/g$ , respectively. In order to better observe the changes of pore structure of shale samples, the pore size distributions and absolute values of pore volume for each type of

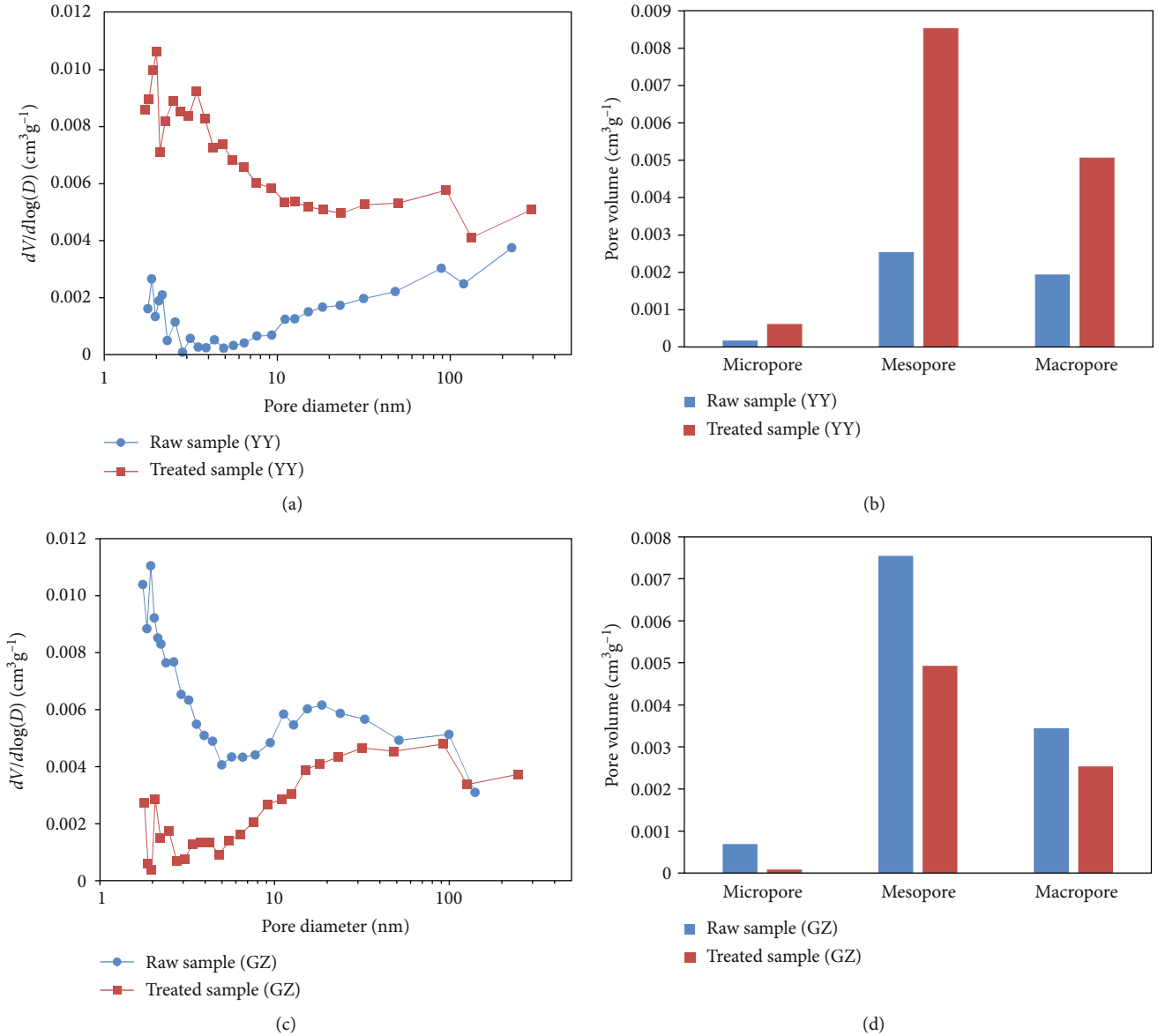


FIGURE 7: Pore size distributions (a, c) and pore volume values (b, d) for each type of pores for the raw and treated shale samples: (a, b) YY; (c, d) GZ.

pores (micropores, mesopores, and macropores) are presented in Figure 7. The pore size distributions of the raw YY and GZ shale revealed that the shale pore structure was multimodal. The YY shale with peaks near 2 nm and 100 nm and the GZ shale with peaks near 2 nm and 10 nm are shown in Figures 7(a) and 7(c). The pore size distributions of the raw YY and GZ shale were different from those of the Barnett shale in North American shale plays and Otter-Park shale in the Horn River Basin [41, 42]. It was observed that the pore size distributions of the YY shale increased significantly after slick water treatment (Figure 7(a)), especially the mesopores (Figure 7(b)). However, the micropores and mesopores of the GZ shale after reaction with slick water were significantly lower than the raw sample (Figures 7(c) and 7(d)).

Combined with the analyses of the FE-SEM and XRD, the increase of the specific surface area and pore volume of YY

shale after reaction with slick water can be attributed to the dissolution of pyrite, which could produce some nanopores. In addition, the  $\text{H}^+$  released from the pyrite dissolution could react with the calcite, resulting in the increase of nanopores. Although the clay swelling may narrow the nanopores in the YY shale, the influence degree was lower than the pyrite dissolution. The changes of pore structures in GZ shale may be related to the dissolution of carbonate minerals and the swelling of clay minerals. As observed by FE-SEM, the dissolution of carbonate minerals changed the micropores and mesopores into larger dissolution pores. Owing to the fact that the apparatus used in the low-temperature  $\text{N}_2$  adsorption analysis only measured the pores with a diameter less than 383 nm, the produced dissolution pores cannot be measured. Moreover, the mixed layer illite/smectite, which was one of the dominant clay minerals in the shale of Niutitang Formation in Youyang County and Northwest Hunan area

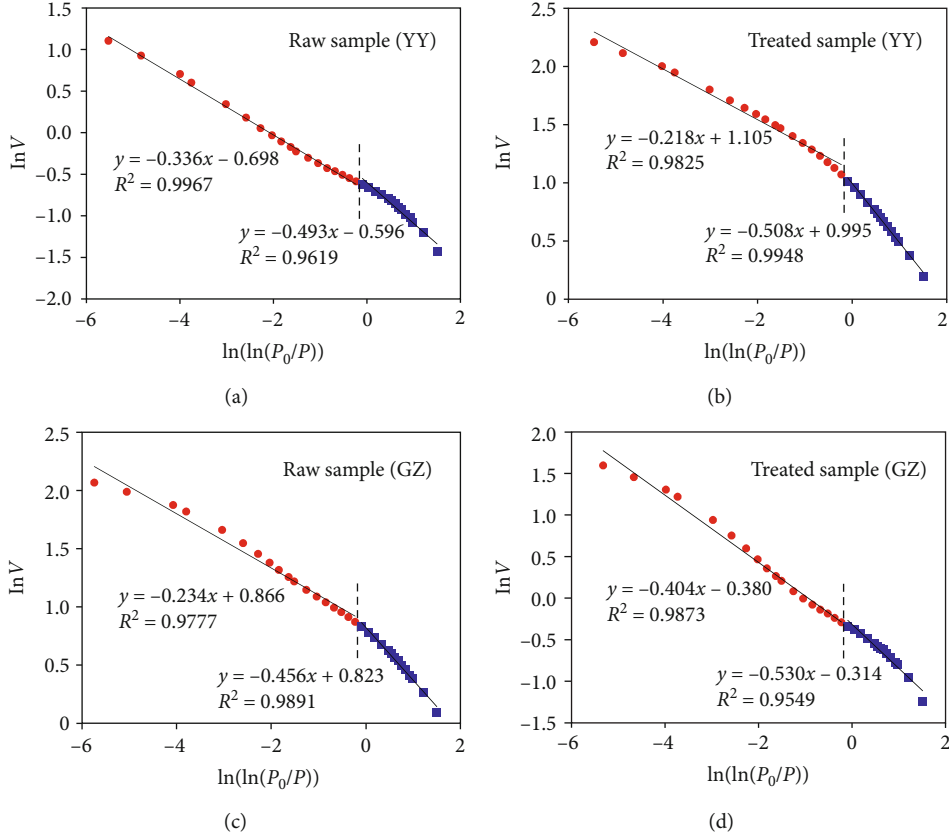


FIGURE 8: Plots of  $\ln(V)$  versus  $\ln(\ln(P_0/P))$  calculated from the  $N_2$  adsorption isotherms of shale samples before and after slick water treatment: (a, b) YY; (c, d) GZ.

[30, 31], could swell and enlarge during shale-fracturing fluid interactions. The clay-swelling effect can reduce the nanopores of GZ shale after reaction.

**3.4. Fractal Analysis.** Fractal analysis is a powerful method to characterize the pore surface irregularities and structural properties of a solid [43, 44]. Owing to the complexity of diagenesis and sedimentation, shale usually has a complex pore structure and irregular pore geometry [45, 46]. The fractal dimension  $D$  can be used to describe the quantitative evaluation of the fractal geometry including the pore structure surface roughness and geometrical irregularity [44]. The fractal dimension  $D$  generally varies between 2 and 3, and the maximum value 3 represents a complex, irregular, or rough surface, while the minimum value 2 represents a perfectly smooth surface [44, 45]. The  $N_2$  adsorption data has been widely used to calculate the fractal dimensions based on the Frenkel-Halsey-Hill (FHH) equation [47–49], and the FHH equation can be described as follows [43]:

$$\ln V = C + (D - 3) \ln \left( \ln \left( \frac{P_0}{P} \right) \right), \quad (7)$$

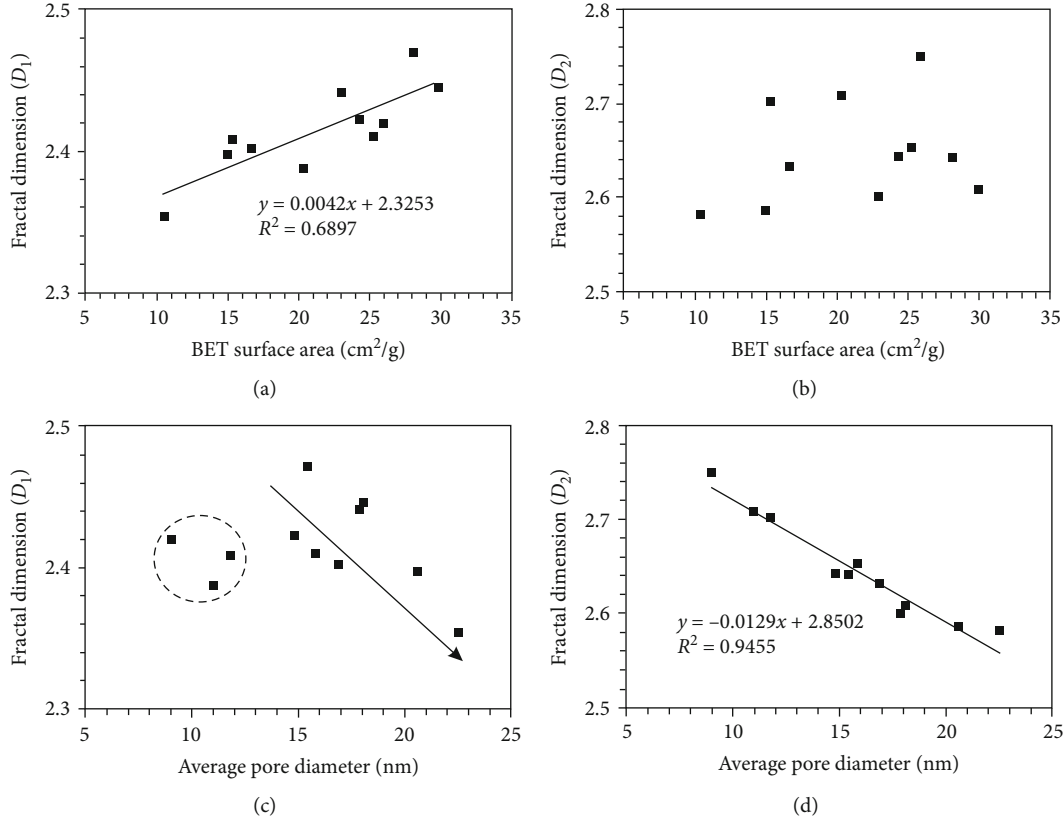
where  $V$  is the adsorption  $N_2$  volume at equilibrium pressure,  $\text{cm}^3/\text{g}$ ;  $C$  is a constant of gas adsorption;  $D$  is the fractal dimension, which can be calculated from the slope of the plot of  $\ln(V)$  versus  $\ln(\ln(P_0/P))$ .

According to the FHH equation, the plots of  $\ln(V)$  -  $\ln(\ln(P_0/P))$  for the two shale samples before and after reaction were obtained (Figure 8). In these plots, two different linear segments were found at relative pressures of 0-0.45 and 0.45-1, indicating that the mechanism of gas adsorption in the two areas was different. At lower relative pressures (0-0.45), the gas adsorption behavior was dominated by Van der Waals forces, while at higher relative pressures (0.45-1), the gas adsorption behavior was dominated by capillary condensations [45]. Therefore, two fractal dimensions  $D_1$  and  $D_2$  were calculated from the relative pressures of 0-0.45 and 0.45-1, respectively (Table 5). The results showed that the correlation coefficients ( $R^2$ ) of the two regions were greater than 0.95, reflecting that the fractal characteristics at the two intervals are different [45]. As illustrated in Table 5, the fractal dimension  $D_1$  of the slick water-treated YY shale decreased, whereas the fractal dimension  $D_2$  increased. However, after the slick water treatment, the fractal dimensions ( $D_1$  and  $D_2$ ) of the GZ shale decreased.

In the previous studies of Ji et al. [47], the  $D_1$  had a good positive relationship with the specific surface area of shale samples, while the relationship between  $D_2$  and specific surface area was ambiguous (Figures 9(a) and 9(b)). The finding reflected that the surface area of shale had a significant impact on  $D_1$ , but not on  $D_2$  [47]. Moreover, the previous studies showed that the fractal dimensions  $D_1$  and  $D_2$  of marine shale had a negative relationship with the average

TABLE 5: Fractal dimensions of the shale samples before and after slick water treatment.

| Samples | State   | $P/P_0$ : 0-0.45      |       |        | $P/P_0$ : 0.45-1      |       |        |
|---------|---------|-----------------------|-------|--------|-----------------------|-------|--------|
|         |         | Fitting equation      | $D_1$ | $R^2$  | Fitting equation      | $D_2$ | $R^2$  |
| YY      | Raw     | $y = -0.493x - 0.596$ | 2.507 | 0.9619 | $y = -0.336x - 0.698$ | 2.664 | 0.9967 |
|         | Treated | $y = -0.508x + 0.995$ | 2.492 | 0.9948 | $y = -0.218x + 1.105$ | 2.782 | 0.9825 |
| GZ      | Raw     | $y = -0.456x + 0.823$ | 2.544 | 0.9891 | $y = -0.234x + 0.866$ | 2.776 | 0.9777 |
|         | Treated | $y = -0.530x - 0.314$ | 2.470 | 0.9549 | $y = -0.404x - 0.380$ | 2.596 | 0.9873 |

FIGURE 9: Plots of  $D_1$  and  $D_2$  versus the BET surface area (a, b) and average pore diameter (c, d) of Longmaxi shale [47].

pore diameters, and the  $D_2$  was more sensitive to the average pore diameter of shale than  $D_1$  (Figures 9(c) and 9(d)) [47, 48]. Owing to more micropores and more throats of the shale with smaller average pore size, the pore structure of shale became more complex and heterogonous and had higher fractal dimension  $D_2$  values [45, 47, 48]. Therefore, the  $D_1$  may represent the pore surface fractal dimension which could reflect the roughness of the pore surface, while the  $D_2$  may represent the pore structure fractal dimension which could reflect the complexity or irregularity of the pore structure.

Based on the variation characteristics of fractal dimensions  $D_1$  and  $D_2$ , the pore surface roughness degree was reduced and the pore structure complexity increased in the YY shale after the slick water treatment. According to the low-temperature  $N_2$  analysis (Figures 7(a) and 7(b)), the pyrite and calcite dissolution formed many mesopores and macropores in the YY shale, causing the pore volume

of mesopores and macropores to increase from  $0.00254 \text{ cm}^3/\text{g}$  to  $0.00854 \text{ cm}^3/\text{g}$  and from  $0.00194 \text{ cm}^3/\text{g}$  to  $0.00507 \text{ cm}^3/\text{g}$ , respectively. These mesopores and macropores formed by the reaction may increase the connectivity of the nanopores in the YY shale and then decrease the surface roughness of shale. Meanwhile, the pyrite dissolution also produced some micropores and increased the specific surface area in the YY shale. A previous study showed that the  $D_2$  and specific surface area had a better correlation [46], which suggested that the increase of pore structure complexity in YY shale may be contributed to the increase of micropores in the shale. In the GZ shale, the changes of  $D_1$  and  $D_2$  reflected that the degree of pore surface roughness and structure complexity decreased after reaction. These changes may be caused by the dissolution of carbonate minerals which developed many dissolution pores and decreased the number of micropores in shale, making the pore structure more smooth and regular.

The fractal dimension changes can affect the methane adsorption and gas production capacity of shale, and a higher fractal dimension  $D_1$  indicates a greater surface area for methane adsorption and increases the methane adsorption capacity of shale [47]. However, a higher fractal dimension  $D_2$  represents a more complex pore structure, causing an easier methane desorption in the shale reservoir and facilitating the gas production from the shale reservoir [47]. Consequently, after the interactions with slick water, the methane adsorption capacity reduced and gas production capacity increased for YY shale; however, the capacity of methane adsorption and gas production of GZ shale may be reduced.

**3.5. Porosity Analysis.** According to the principle of helium gas expansion, the porosity of the two shale samples before and after reaction was measured. In order to eliminate the effect of sample heterogeneity, the same sample was used before and after reaction. The porosity of the raw YY shale was 4.40%, and after slick water treatment for three days, the porosity changed to 4.48% which showed slight increase. Conversely, the porosity of the GZ shale showed a decreasing trend after reaction, changing from 2.93% to 2.41%.

The porosity changes of the YY shale may be attributed to the dissolution of pyrite, which created some nanopores in shale. In addition, the slight increase of porosity may be related to the extent of pyrite dissolution. The pyrite dissolution could be inhibited owing to the exhaustion of the oxygen supply in the reactor [50]. In our experiments, the reactor was sealed during the reaction and the dissolved oxygen only came from the slick water fracturing fluid. Combined with equations (1) and (2), it can be seen that the pyrite dissolution may be self-limiting as a result of the consumption of oxygen. Unlike the carbonate-poor shale, the calcite and dolomite were filled in the areas between quartz and clay minerals (Figures 3(a) and 3(b)) in the GZ shale. Although the dissolution of carbonate minerals generated a rough spongy texture and some dissolution pores on the surface of GZ shale, the porosity showed a decreasing trend. In the study of Harrison et al. [50], the connectivity and distribution of the porosity generated by the dissolution of carbonate minerals depended on the distribution of carbonate minerals. The isolated carbonate mineral grains tended to develop discrete pores, while the homogeneous carbonate mineral distribution tended to generate a spongy and mottled texture and develop a pervasive secondary porosity network [50]. Based on the FE-SEM observation, the GZ shale only generated some discrete pores and stripes after reaction with slick water fracturing fluid, and owing to the distribution of isolated carbonate minerals, it did not generate the connectively secondary porosity network (Figures 3(c) and 3(d)). Moreover, the carbonate dissolution resulted in the collapse of the shale surface (Figure 3(d)), which could inhibit the gas and fluid transport in the shale reservoir [50] and cause the porosity of shale decrease. Owing to the carbonate dissolution of carbonate-rich GZ shale, the distribution characteristic of pore sizes and types after reaction was altered, and thus, the porosity of the shale matrix was reduced.

## 4. Conclusions

In this paper, two different mineral composition shale samples were used to investigate the effect of initial shale mineralogy on the pore structure characteristic evolution during hydraulic fracturing. The changes of mineral composition and pore structure characteristics of the shale samples were measured using FE-SEM, XRD, low-temperature  $N_2$  adsorption, and porosity measurement. The conclusions drawn from this study are summarized as follows:

- (1) In the carbonate-poor YY shale, the oxidation processes of pyrite occurred after reaction with the slick water. The dissolution of pyrite generated some dissolution nanopores and led to the significant increase of the specific surface area and the total pore volume; the pore surface became less rough, while the pore structure became more complex. Moreover, the porosity of shale increased from 4.40% to 4.48%
- (2) In the carbonate-rich GZ shale, the carbonate dissolution occurred owing to the hydrolysis of the AMPS in the slick water. The carbonate dissolution transformed the micropores and mesopores into larger dissolution pores and led to the decrease of the specific surface area and the total pore volume of nanopores, and the pore surface and structure became more smooth and regular. However, the carbonate dissolution only generated some isolated dissolution pores and stripes. As a result, the porosity of the shale matrix was reduced
- (3) The pore structure alteration of different mineralogical composition shale may be related to different pH-buffering capacities of the shale. The carbonate-poor shale had low pH-buffering capacity, causing the fluid pH to remain acidic during reaction. However, the carbonate-rich shale had high pH-buffering capacity, which rapidly recovered the pH value of the fluid to neutral-alkaline conditions. The results of this study illustrated that the initial mineral compositions of shale could affect the pore structure characteristics of shale during hydraulic fracturing, and the additives of fracturing fluid should be adjusted according to shale mineralogy

## Data Availability

The data used to support the findings of this study are included within the article.

## Conflicts of Interest

The authors declare that they have no conflicts of interest.

## Acknowledgments

This study was supported by the National Natural Science Foundation of China (No. 41831176), the Excellent Doctors Come to Shanxi to Reward Scientific Research Projects

(No. SXYBKY2018027), the Chinese Academy of Sciences Key Project (No. XDB26020302), and the National Key R&D Program of China (No. 2017YFA0604803).

## References

- [1] R. D. Vidic, S. L. Brantley, J. M. Vandenbossche, D. Yoxtheimer, and J. D. Abad, "Impact of shale gas development on regional water quality," *Science*, vol. 340, article 1235009, 2013.
- [2] R. A. Kerr, "Natural gas from shale bursts onto the scene," *Science*, vol. 328, pp. 1624–1626, 2010.
- [3] EIA, "Natural gas: data," <https://www.eia.gov/analysis/studies/worldshalegas/>.
- [4] P. J. M. Monteiro, C. H. Rycroft, and G. I. Barenblatt, "A mathematical model of fluid and gas flow in nanoporous media," *Proceedings of the National Academy of Sciences of the United States of America*, vol. 109, pp. 20309–20313, 2012.
- [5] J. Dai, C. Zou, D. Dong et al., "Geochemical characteristics of marine and terrestrial shale gas in China," *Marine and Petroleum Geology*, vol. 76, pp. 444–463, 2016.
- [6] M. Zheng, J. Li, X. Wu et al., "China's conventional and unconventional natural gas resources: potential and exploration targets," *Journal of Natural Gas Geoscience*, vol. 3, pp. 295–309, 2018.
- [7] Z. Chong, Q. Yao, and X. Li, "Effect of joint geometrical parameters on hydraulic fracture network propagation in naturally jointed shale reservoirs," *Geofluids*, vol. 2018, Article ID 1852604, 23 pages, 2018.
- [8] T. Engelder, L. M. Cathles, and L. T. Bryndzia, "The fate of residual treatment water in gas shale," *Journal of Unconventional Oil and Gas Resources*, vol. 7, pp. 33–48, 2014.
- [9] Y. Shen, H. Ge, C. Li et al., "Water imbibition of shale and its potential influence on shale gas recovery—a comparative study of marine and continental shale formations," *Journal of Natural Gas Science and Engineering*, vol. 35, pp. 1121–1128, 2016.
- [10] M. Ali and B. Hascakir, "A critical review of emerging challenges for the oil field waters in the United States," in *SPE E&P Health, Safety, Security and Environmental Conference—Americas*, Denver, CO, USA, 2015.
- [11] X. Huang and Y. Zhao, "Characterization of pore structure, gas adsorption, and spontaneous imbibition in shale gas reservoirs," *Journal of Petroleum Science and Engineering*, vol. 159, pp. 197–204, 2017.
- [12] B. Roychaudhuri, T. T. Tsotsis, and K. Jessen, "An experimental investigation of spontaneous imbibition in gas shales," *Journal of Petroleum Science and Engineering*, vol. 111, pp. 87–97, 2013.
- [13] N. Chakraborty, Z. T. Karpyn, S. Liu, and H. Yoon, "Permeability evolution of shale during spontaneous imbibition," *Journal of Natural Gas Science and Engineering*, vol. 38, pp. 590–596, 2017.
- [14] T. Zhou, S. Zhang, L. Yang, X. Ma, Y. Zou, and H. Lin, "Experimental investigation on fracture surface strength softening induced by fracturing fluid imbibition and its impacts on flow conductivity in shale reservoirs," *Journal of Natural Gas Science and Engineering*, vol. 36, pp. 893–905, 2016.
- [15] L. Wang, J. D. Fortner, and D. E. Giammar, "Impact of water chemistry on element mobilization from Eagle Ford Shale," *Environmental Engineering Science*, vol. 32, pp. 310–320, 2015.
- [16] A. Zolfaghari, Y. Z. Tang, J. Holyk, M. Binazadeh, and H. Dehghanpour, "Advances in flowback chemical analysis of gas shales," in *SPE Annual Technical Conference and Exhibition*, Houston, TX, USA, 2015.
- [17] A. Zolfaghari, H. Dehghanpour, M. Noel, and D. Beariger, "Laboratory and field analysis of flowback water from gas shales," *Journal of Unconventional Oil and Gas Resources*, vol. 14, pp. 113–127, 2016.
- [18] A. Zolfaghari and H. Dehghanpour, "Produced flowback salts vs. induced-fracture interface: a field and laboratory study," *SPE Journal*, vol. 24, pp. 1309–1321, 2019.
- [19] M. Xu, M. Binazadeh, A. Zolfaghari, and H. Dehghanpour, "Effects of dissolved oxygen on water imbibition in gas shales," *Energy & Fuels*, vol. 32, pp. 695–4704, 2018.
- [20] W. T. Stringfellow, J. K. Domen, M. K. Camarillo, W. L. Sandelin, and S. Borglin, "Physical, chemical, and biological characteristics of compounds used in hydraulic fracturing," *Journal of Hazardous Materials*, vol. 275, pp. 37–54, 2014.
- [21] Z. Sun, H. Zhang, Z. Wei et al., "Effects of slick water fracturing fluid on pore structure and adsorption characteristics of shale reservoir rocks," *Journal of Natural Gas Science and Engineering*, vol. 51, pp. 27–36, 2018.
- [22] J. Guo, Y. Li, and S. Wang, "Adsorption damage and control measures of slick-water fracturing fluid in shale reservoirs," *Petroleum Exploration and Development*, vol. 45, pp. 336–342, 2018.
- [23] J. K. Pearce, L. Turner, and D. Pandey, "Experimental and predicted geochemical shale-water reactions: Roseneath and Murteree shales of the Cooper Basin," *International Journal of Coal Geology*, vol. 187, pp. 30–44, 2018.
- [24] Q. Li, A. Jew, A. Kiss et al., "Imaging pyrite oxidation and barite precipitation in gas and oil shales," in *SPE/AAPG/SEG Unconventional Resources Technology Conference*, Houston, TX, USA, 2018.
- [25] C. Wu, J. Tuo, M. Zhang, L. Sun, Y. Qian, and Y. Liu, "Sedimentary and residual gas geochemical characteristics of the Lower Cambrian organic-rich shales in Southeastern Chongqing, China," *Marine and Petroleum Geology*, vol. 75, pp. 140–150, 2016.
- [26] Z. Yang, G. Teng, and Z. Li, "An example of shale gas selected marine area model of Lower Cambrian on the middle and upper Yangtze," *Natural Gas Geoscience*, vol. 22, pp. 8–14, 2011.
- [27] G. Li, D. Bai, X. Wang, P. Luo, W. Jiang, and X. Xiong, "Exploration prospect of the Cambrian Niutitang Formation shale gas in northwestern Hunan," *Geology Survey of China*, vol. 2, pp. 31–39, 2015.
- [28] S. Brunauer, P. H. Emmett, and E. Teller, "Adsorption of gases in multimolecular layers," *Journal of the American Chemical Society*, vol. 60, article 10.1021/ja01269a023, pp. 309–319, 1938.
- [29] E. P. Barrett, L. G. Joyner, and P. P. Halenda, "The determination of pore volume and area distributions in porous substances. I. Computations from nitrogen isotherms," *Journal of the American Chemical Society*, vol. 73, pp. 373–380, 1951.
- [30] X. Cao, B. Yu, X. Li, M. Sun, and L. Zhang, "Reservoir characteristics and well-logging evaluation of the Lower Cambrian shales in southeast Chongqing, China," *Petroleum Research*, vol. 1, pp. 178–190, 2016.
- [31] P. Jiao, J. Guo, X. Wang, and C. Liu, "Characteristics and significance of petrological-mineralogical of Lower Cambrian Niutitang Formation shale gas reservoir in northwest Hunan,"

- Journal of Central South University (Science and Technology)*, vol. 49, pp. 1447–1458, 2018.
- [32] A. Sanaei, M. Shakiba, A. Varavei, and K. Sepehrnoori, “Mechanistic modeling of clay swelling in hydraulic-fractures network,” *SPE Reservoir Evaluation & Engineering*, vol. 21, 2018.
- [33] E. Rowan, M. Engle, T. Kraemer, K. Schroeder, R. Hammack, and M. Doughten, “Geochemical and isotopic evolution of water produced from middle Devonian Marcellus shale gas wells, Appalachian Basin, Pennsylvania,” *AAPG Bulletin*, vol. 99, pp. 181–206, 2015.
- [34] Q. Chen, Y. Kang, L. You, P. Yang, X. Zhang, and Q. Cheng, “Change in composition and pore structure of Longmaxi black shale during oxidative dissolution,” *International Journal of Coal Geology*, vol. 172, pp. 95–111, 2017.
- [35] P. Singer and W. Stumm, “Acidic mine drainage: the rate-determining step,” *Science*, vol. 167, pp. 1121–1123, 1970.
- [36] J. A. Chermak and M. E. Schreiber, “Mineralogy and trace element geochemistry of gas shales in the United States: environmental implications,” *International Journal of Coal Geology*, vol. 126, pp. 32–44, 2014.
- [37] C. Descourvières, N. Hartog, B. M. Patterson, C. Oldham, and H. Prommer, “Geochemical controls on sediment reactivity and buffering processes in a heterogeneous aquifer,” *Applied Geochemistry*, vol. 25, pp. 261–275, 2010.
- [38] A. D. Jew, M. K. Dustin, A. L. Harrison et al., “Impact of organics and carbonates on the oxidation and precipitation of iron during hydraulic fracturing of shale,” *Energy & Fuels*, vol. 31, pp. 3643–3658, 2017.
- [39] L. Sun, J. Tuo, M. Zhang, C. Wu, Z. Wang, and Y. Zheng, “Formation and development of the pore structure in Chang 7 member oil-shale from Ordos Basin during organic matter evolution induced by hydrous pyrolysis,” *Fuel*, vol. 158, pp. 549–557, 2015.
- [40] K. S. W. Sing, “Reporting physisorption data for gas/solid systems with special reference to the determination of surface area and porosity (Recommendations 1984),” *Pure and Applied Chemistry*, vol. 57, pp. 603–619, 1985.
- [41] C. R. Clarkson, N. Solano, R. M. Bustin et al., “Pore structure characterization of North American shale gas reservoirs using USANS/SANS, gas adsorption, and mercury intrusion,” *Fuel*, vol. 103, pp. 606–616, 2013.
- [42] A. Zolfaghari, H. Dehghanpour, and M. Xu, “Water sorption behaviour of gas shales: II. Pore size distribution,” *International Journal of Coal Geology*, vol. 179, pp. 187–195, 2017.
- [43] D. Avnir and M. Jaroniec, “An isotherm equation for adsorption on fractal surfaces of heterogeneous porous materials,” *Langmuir*, vol. 5, pp. 1431–1433, 1989.
- [44] P. Pfeifer and D. Avnir, “Chemistry noninteger dimensions between two and three,” *Journal of Chemical Physics*, vol. 79, pp. 3369–3558, 1983.
- [45] Y. Yao, D. Liu, D. Tang, S. Tang, and W. Huang, “Fractal characterization of adsorption-pores of coals from North China: an investigation on CH<sub>4</sub> adsorption capacity of coals,” *International Journal of Coal Geology*, vol. 73, pp. 27–42, 2008.
- [46] X. Shao, X. Pang, and Q. Li, “Pore structure and fractal characteristics of organic-rich shales: a case study of the lower Silurian Longmaxi shales in the Sichuan Basin, SW China,” *Marine and Petroleum Geology*, vol. 80, pp. 192–202, 2017.
- [47] W. Ji, Y. Song, Z. Jiang et al., “Fractal characteristics of nanopores in the Lower Silurian Longmaxi shales from the Upper Yangtze Platform, South China,” *Marine and Petroleum Geology*, vol. 78, pp. 88–98, 2016.
- [48] L. Liang, J. Xiong, and X. Liu, “An investigation of the fractal characteristics of the upper Ordovician Wufeng Formation shale using nitrogen adsorption analysis,” *Journal of Natural Gas Science and Engineering*, vol. 27, pp. 402–409, 2015.
- [49] C. Yang, J. Zhang, X. Wang et al., “Nanoscale pore structure and fractal characteristics of a marine-continental transitional shale: a case study from the lower Permian Shanxi shale in the southeastern Ordos Basin, China,” *Marine and Petroleum Geology*, vol. 88, pp. 54–68, 2017.
- [50] A. L. Harrison, A. D. Jew, M. K. Dustin et al., “Element release and reaction-induced porosity alteration during shale-hydraulic fracturing fluid interactions,” *Applied Geochemistry*, vol. 82, pp. 47–62, 2017.



**Hindawi**

Submit your manuscripts at  
[www.hindawi.com](http://www.hindawi.com)

